Observation of signature partner bands in ^{117}Sb

R. Banik,[1,2] S. Bhattacharyya,[1,2,*] Soumik Bhattacharya,[1,2] G. Mukherjee,[1,2] R. Goswami,[3] D. Choudhury,[3] S. Das,[4] S. Samanta,[4] S. S. Ghugre,[4] R. Raut,[4] and A. Goswami[5]

[1]*Variable Energy Cyclotron Centre, 1/AF Bidhannagar, Kolkata 700064, India*
[2]*Homi Bhabha National Institute, Training School Complex, Anushaktinagar, Mumbai 400094, India*
[3]*B.P. Poddar Institute of Management and Technology, Kolkata 700052, India*
[4]*UGC-DAE CSR, Kolkata Centre, Kolkata 700098, India*
[5]*Saha Institute of Nuclear Physics, 1/AF, Bidhannagar, Kolkata 700064, India*

(Received 30 April 2019; revised manuscript received 29 October 2019; published 27 January 2020)

Rotational band structures and low-lying single-particle levels in ^{117}Sb have been populated using reaction ^{115}In(α, $2n$) ^{117}Sb at a beam energy of 28 MeV and investigated using γ-ray spectroscopic techniques. The existing level scheme has been extended with the observation of 31 new transitions. The signature partner of the band structure based on the configuration of $\pi g_{7/2} \otimes$ 2p-2h of the ^{116}Sn core has been established in ^{117}Sb for the first time. Several single-particle nonyrast transitions connecting to various band structures have also been identified. Measurements of the DCO ratios, polarization asymmetry and angular distribution of the observed γ rays have been carried out to assign the spin-parities to the levels of all the band structures and the low-lying single-particle states, populated in the present work. The spin-parities are also determined for the states of the two previously unassigned bands. The lower-spin structures have been interpreted on the basis of large-scale shell-model calculations using OXBASH. Particle Rotor Model (PRM) calculations have been carried out to explain the large signature splitting of the observed signature partner bands.

DOI: 10.1103/PhysRevC.101.014322

I. INTRODUCTION

Nuclei with proton number near to the shell closure and neutron number at the midshell are known to demonstrate single-particle excitations as well as collective behaviors depending on various angular momentum couplings among the valence nucleons and the core. In that context, Sb isotopes ($Z = 51$) of the $A \approx 110$–120 region with one valence proton particle above the $Z = 50$ shell closure are the ideal candidates for the understanding of such competition between collectivity and single-particle yrast and near-yrast excitations [1,2]. The properties of the Sb nuclei in the above mass region provide the link between the spherical magic Sn nuclei and the transitional nuclei with $Z \geqslant 52$. The level structures of the even-even core of Sn nuclei in this mass region show both single-particle and collective excitations. Deformed rotational structures in Sn nuclei have been interpreted as due to the proton two-particle–two-hole (2p-2h) excitations across the $Z = 50$ shell closure as reported, for example, in ^{116}Sn [3]. Structures involving a valence proton coupled to both spherical and deformed states of the corresponding Sn core have been observed systematically in odd-A Sb isotopes in this mass region [4–7]. Since the Sb nuclei have only one valence proton beyond the shell closure at $Z = 50$, the low-spin structures in odd-mass Sb nuclei are expected to be understood as single-particle excitations. At higher spin, in addition to the single-particle states, excitation of a proton beyond the $Z = 50$ shell closure, giving rise to two-particle–one-hole (2p-1h) states, are observed in all odd-A Sb isotopes of the mass $A \approx 110$–120 region. In each of these Sb isotopes [8,9], a $9/2^+$ state has been identified and interpreted as deformed 2p-1h state of configuration $(\pi g_{7/2})^2 \otimes (\pi g_{9/2})^{-1}$, originating from a proton excitation from the up-sloping $g_{9/2}$ orbital to the down-sloping $g_{7/2}$ orbital, across the $Z = 50$ core. This $9/2^+$ state forms the band head of the strongly coupled rotational band consisting of strong $\Delta J = 1$ transitions in odd-A Sb isotopes [6,7,10] demonstrating the deformation-driving effect of the $g_{9/2}$ intruder orbital. Involvement of the $\pi h_{11/2}$ intruder orbital, on the other hand, enforces rather enhanced deformation which is manifested in the observation of negative-parity rotational bands at relatively higher excitation energy with larger moment of inertia in the odd mass Sb isotopes [11,12]. The typical deformation (β_2) of such bands was found to be $\approx$0.32 for ^{113}Sb [5,11].

The lowest-lying two positive-parity proton orbitals above $Z = 50$, namely $\pi d_{5/2}$ and $\pi g_{7/2}$, lie very close to each other and are expected to be highly mixed at small deformation. Accordingly, the ground-state spin and parity of the neutron-deficient odd-A Sb isotopes are $J^\pi = 5/2^+$ and a level with $J^\pi = 7/2^+$ lies close to it. The energy difference between these two levels decreases with increasing neutron number and the $J^\pi = 7/2^+$ becomes the ground state for the neutron rich isotopes with $A \geqslant 123$. Deformed rotational band structures, built on these proton states, coupled with the 2p-2h Sn core states, are also expected to be observed in the odd-A Sb

*Corresponding author: sarmi@vecc.gov.in

isotopes at relatively low excitation energies. In contrast to the $g_{9/2}$ bands, these rotational bands would have $\Delta J = 2$ structure along with a signature partner and have large signature splitting because of the involvement of the low-Ω Nilsson components of these orbitals. From the measured signature splitting it is possible to understand the nature of the coupling of the odd-proton with the core and thereby the involved Nilsson configuration of the band. Such bands have been well investigated in the odd-*A* I ($Z = 53$) isotopes [13] and also in some Cs ($Z = 55$) isotopes [14] but are not well investigated in the odd-*A* Sb isotopes. However, in the I and Cs nuclei, the proton Fermi level of the even-even core already lies above the $Z = 50$ shell gap. Therefore, a detailed investigation of the band structures built on the $\pi d_{5/2}$ and $\pi g_{7/2}$ orbitals in the odd-*A* Sb isotopes is important and will provide information on the shape-polarizing effect of these orbitals on a $Z = 50$ even-even core and the lowest excitation energy at which the deformed structure is realized in Sb nuclei. Indication of bandlike structure based on $\pi g_{7/2}$ has been observed only in ^{117,119}Sb isotopes [7] but since no signature partner bands were identified, a detailed characterization of these bands was not possible.

Initial studies on ^{117}Sb were from β decay of ^{117}Te, which are restricted to low-spin states [15]. Experimental investigations have also been carried out using α-, deuteron-, and proton-induced reactions with only a few Ge(Li) detectors [16–19]. Shape coexistence in ^{117}Sb at a comparatively higher spin was predicted from the presence of an isomer at the $23/2^-$ level [20]. The high-spin excited levels of ^{117}Sb have been investigated from the (^{11}B, $4n$) reaction with six Compton-suppressed HPGe detectors [7]. But the use of HPGe detectors in this study did not allow to obtain polarization information of the observed γ rays. With the availability of the new-generation array of Clover HPGe detectors, it is now possible to have high-resolution spectroscopic information with better γ-γ coincidence efficiency and spin-parity assignment of excited states from the Ratio of the Directional Correlation from Oriented states (R_{DCO}) and polarization measurements.

In the present work, we report here the study of the excited states in ^{117}Sb using α-induced reaction. The primary motivation in this work was to identify and to study the $g_{7/2}$ band in ^{117}Sb in order to investigate the shape-driving effect of this orbital on the even-even Sn core. Moreover, the importance of the two lowest-lying orbitals, $g_{7/2}$ and $d_{5/2}$, lying just above the $Z = 50$ gap, in generating the low-lying single-particle states in ^{117}Sb has also been reported.

II. EXPERIMENT

The high-spin excited states of ^{117}Sb have been populated using the fusion-evaporation reaction ^{115}In(α, $2n$) ^{117}Sb at a beam energy of 28 MeV. The α beam was delivered from the K-130 cyclotron at Variable Energy Cyclotron Centre, Kolkata, India. A 4.1-mg/cm^2-thick $^{nat.}$In self-supporting foil was used as the target. The $^{nat.}$In consists of two isotopes of $A = 113$ and 115, of which the abundance of $A = 115$ is 95.7%. It is estimated that the $2n$ channel is the most dominant (≈90% of total fusion cross section) at this beam energy with

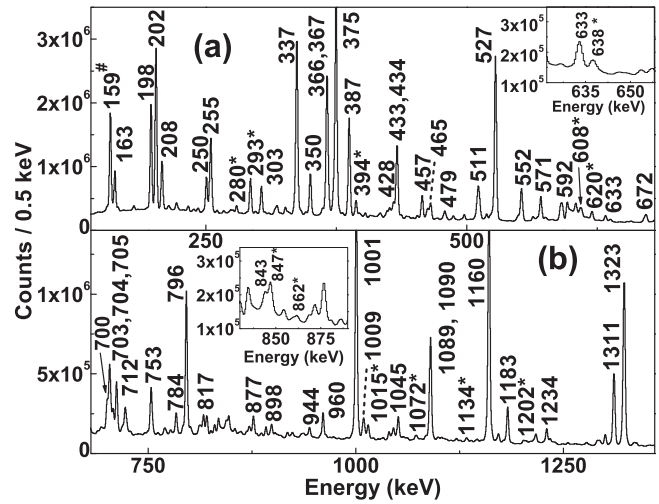

FIG. 1. Total projection of the E_γ-E_γ matrix, as obtained in the present experiment. All the γ rays marked in the figure are from ^{117}Sb. The spectrum is shown in two parts: (a) up to 680 keV and (b) beyond 680 keV. The newly observed transitions from the present work are marked with "∗." The insets show some of the new transitions in an expanded scale. The 159-keV γ ray, marked with "#" is from ^{117}Sn, populated from the decay of ^{117}Sb.

a cross section of the order of 1 barn. The γ rays were detected using VEcc array for NUclear Spectroscopy (VENUS) [21,22] setup, consisting of six Compton suppressed HPGe Clover detectors. The detectors were placed in the median plane around the target position with one detector each at forward 45° and 55°, two at 90°, and two at backward 30° angles with respect to the beam direction. The Clover detectors were placed at a distance of 26 cm from the target position. The pulse processing and data acquisition system was based on PIXIE-16 250-MHz 12-bit digitizer modules fabricated by XIA LLC (USA) and working on firmware conceptualized by UGC-DAE CSR, Kolkata Centre [23]. Time-stamped list mode data were acquired under the event trigger condition based on Compton suppressed Clover detector multiplicity (M_γ) set either in singles ($M_\gamma \geqslant 1$) or in coincidence ($M_\gamma \geqslant 2$) mode. The energy and efficiency calibration of each Clover detector were carried out using standard ^{133}Ba and ^{152}Eu radioactive sources, placed at the target position.

III. DATA ANALYSIS

The acquired data were sorted using the IUCPIX package [23], developed by UGC-DAE CSR (Kolkata Centre) to construct symmetric and angle-dependent (asymmetric) E_γ-E_γ matrices and E_γ-E_γ-E_γ cube, and were subsequently analyzed using RADWARE [24] and LAMPS [25] analysis packages. Details of these data-sorting programs can be found in Ref. [23]. Figure 1 represents the total projection of the E_γ-E_γ symmetric matrix as obtained in the present experiment. All the γ rays marked in Fig. 1 are from ^{117}Sb, which is the dominant or almost singly populated channel in the α-induced reaction used for the present experiment. The level structure of the nucleus of interest was constructed from the coincidence relationships between the observed γ-ray transitions and their

intensities as well as from determining their multipolarities and the electromagnetic character.

The Ratio of the Directional Correlation from Oriented ($R_{\rm DCO}$) nuclei [26], for assignment of multipolarities to the observed transitions, was determined from an asymmetric E_γ-E_γ matrix, with the x axis containing the data from the 90° (θ_1) detectors and the y axis containing the data from the 30° (θ_2) detectors. The $R_{\rm DCO}$ of a transition (γ_1) is defined as:

$$R_{\rm DCO} = \frac{I_{\gamma_1} \text{ at } \theta_1 (\text{gated by } \gamma_2 \text{ at } \theta_2)}{I_{\gamma_1} \text{ at } \theta_2 (\text{gated by } \gamma_2 \text{ at } \theta_1)}. \quad (1)$$

For a pure stretched quadrupole or dipole transition, the $R_{\rm DCO}$ should be close to unity, when gated by a transition of same multipolarity. On the other hand, if the gating transition is of different multipolarity, then the $R_{\rm DCO}$ value depends on the nature of the gating transition. In the present analysis, the typical value of $R_{\rm DCO}$ is obtained as ≈0.6 for a pure stretched dipole transition when gated with a stretched pure quadrupole transition, whereas for a stretched dipole gate, the corresponding value is found to be ≈1.8 for a pure stretched quadrupole transition.

In addition to the $R_{\rm DCO}$ analysis, the angular distribution of some of the γ rays were also obtained from the data acquired in singles mode (with event trigger set on Compton suppressed Clover detector multiplicity $\geqslant$1). For this purpose, the intensity distribution of the γ rays at different angles are fitted with the Legendre polynomial function,

$$W(\theta) = a_0[1 + a_2 P_2(\cos\theta) + a_4 P_4(\cos\theta)], \quad (2)$$

where θ is the detector angle with respect to the beam axis, a_0 is the normalization parameter, and a_2, a_4 are the angular distribution coefficients. The values of a_2 and a_4 are then used to obtain the multipolarities of the γ rays.

The parity of most of the excited states could be assigned from the polarization measurements of the decaying γ rays by exploiting the close-pack configuration of the Clover detector. The electric or magnetic nature of the observed transitions are obtained from the measurement of the Polarization Directional Correlation from Oriented states (PDCO), as described in Refs. [27,28]. Two 90° Compton suppressed Clover detectors of the VENUS setup were used for polarization asymmetry measurements. The polarization asymmetry parameter ($\Delta_{\rm PDCO}$) is defined as

$$\Delta_{\rm PDCO} = \frac{a(E_\gamma) N_\perp - N_\parallel}{a(E_\gamma) N_\perp + N_\parallel}, \quad (3)$$

where $N_\parallel$ and $N_\perp$ are the counts corresponding to the Compton scattered events of a γ ray in the parallel and perpendicular planes with respect to the reaction plane, respectively. Here $a(E_\gamma)$, defined as $a(E_\gamma) = N_\parallel / N_\perp$, is the geometrical asymmetry correction factor of the detector array. This factor $a(E_\gamma)$, which should be close to unity, can be obtained by using the Compton scattered components of the γ rays from an unpolarized source. For the present experiment, the decay radiations from ^{133}Ba and ^{152}Eu radioactive sources were used to extract the value of $a(E_\gamma)$ from the fitting of its variation as a function of γ-ray energy (E_γ) using the equation $a(E_\gamma) = a_0 + a_1 E_\gamma$. The values of the coefficients are obtained as $a_0 = 1.01(1)$ and $a_1 = 1.37(4) \times 10^{-5}$. In order to get the parallel and perpendicular scattered component of a γ ray, two asymmetric E_γ-E_γ matrices, having parallel and perpendicular scattered events of the 90° Clover detectors along y axis and events from all the other detectors along x axis, were constructed. From the coincidence gate of a γ ray on x axis (corresponding to events from all the detectors), of the above two matrices, the number of counts in the perpendicular ($N_\perp$) and parallel ($N_\parallel$) scattering for a given γ ray were obtained. The positive and negative values of $\Delta_{\rm PDCO}$ correspond to the electric and magnetic character of the scattered γ ray respectively.

IV. RESULTS

The proposed new level scheme of ^{117}Sb from current work is shown in Fig. 2. The band structures in the level scheme are denoted as B1, B1(a), B1(b), B2, B3, B4, B5(a), B5(b), B6, B6(a), and B6(b) for convenience of describing them. The level scheme is extended compared to the previous study with the observation of 31 new γ transitions. The present work reports the bands B1 and B1(a) as the signature partner bands along with the interconnecting transitions between them. Several other single-particle nonyrast excited levels at the low- and medium-spin regions are also identified from the present measurements. Other band structures of B2, B3, B4, and B5, reported previously [7], are also observed in the present work. The tentative spin-parity assignments of the higher-spin states of these band structures have been confirmed in the present work from the $R_{\rm DCO}$ and polarization asymmetry measurements.

The γ rays observed in the present work along with their intensities and spin-parity assignments are tabulated in Table I. The γ rays with $R_{\rm DCO}$ values in the range of 0.5 to 0.7 obtained in a quadrupole gate and 0.9 to 1.1 in a dipole gate with negative $\Delta_{\rm PDCO}$ values are considered as dominantly $M1$ with possible small $E2$ admixture and are assigned as $M1(+E2)$. The γ rays with $R_{\rm DCO}$ values outside the above range and with negative $\Delta_{\rm PDCO}$ values are considered to be of mixed nature and assigned as $M1 + E2$. Figure 3 shows the $R_{\rm DCO}$ vs. $\Delta_{\rm PDCO}$ plot of the newly observed γ rays in the present work along with some of the known γ rays. The nature of the known transitions of ^{117}Sb are well reproduced from the present analysis (shown in red color in Fig. 3). Figure 4 represents the angular distribution of some of the stretched quadrupole and stretched dipole transitions from the current data. Figures 4(a) and 4(c) represent the angular distribution of the known quadrupole transitions of 1160 ($9/2^+ \rightarrow 5/2^+$) and 817 keV ($15/2^+ \rightarrow 11/2^+$) of the bands B5 and B1, respectively. In Figs. 4(b) and 4(d), the angular distribution of the known dipole transitions of 527 ($7/2^+ \rightarrow 5/2^+$) and 163 keV ($11/2^- \rightarrow 9/2^+$) are shown. The angular distribution of 843-keV γ ray of band B1(a), as shown in Fig. 4(e), establishes this transition as a quadrupole, which was not determined earlier. Similarly, the angular distribution of the 638-keV transition, from the new sequence B1(b), is shown in Fig. 4(g). Figures 4(f) and 4(h) represent the angular distribution of the newly observed γ rays of 394 keV of B6(a)

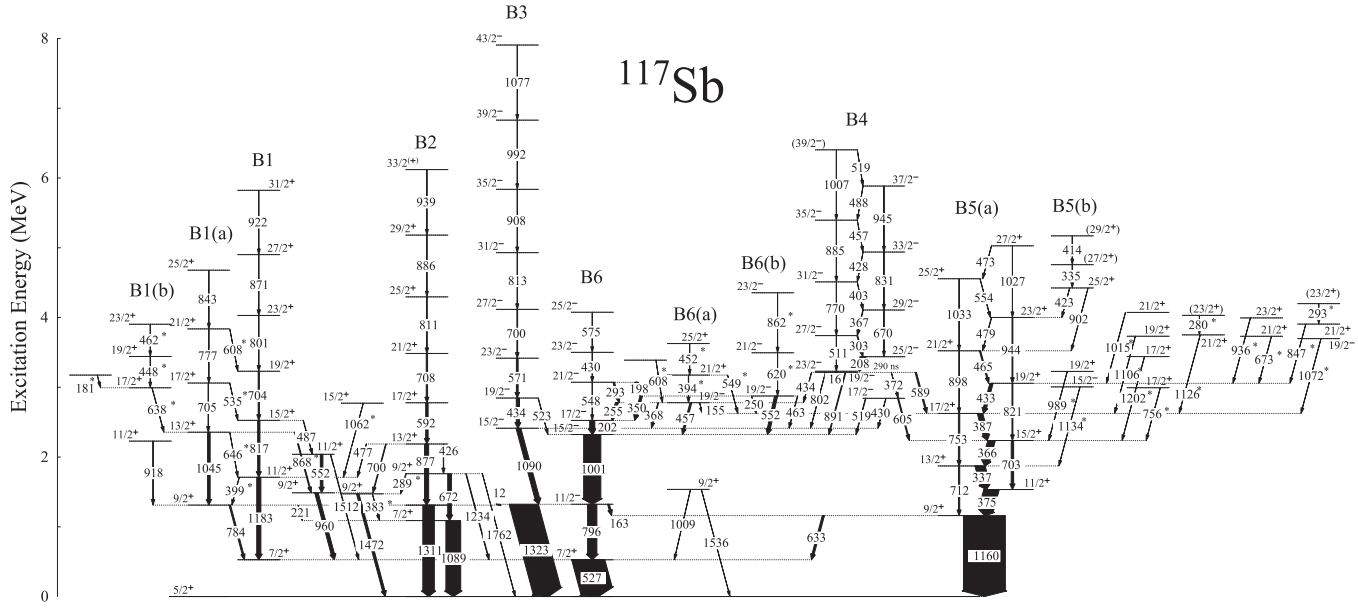

FIG. 2. Proposed level scheme of ^{117}Sb, as obtained from the present work. The new γ rays observed from the present work are marked with $*$ on the right side of the γ-ray energy label.

and 862 keV of B6(b), respectively, which confirm these γ rays as of dipole nature.

In the present work, the band B1 and B1(a) are observed to $31/2^+$ and $25/2^+$ respectively with confirmed spin-parity assignments from $R_{\rm DCO}$ and polarization asymmetry ($\Delta_{\rm PDCO}$) measurements. Though the transitions of these bands were reported previously [7], the spin-parities were assigned only to $27/2^+$ of B1 and $13/2^+$ of B1(a). The DCO ratios of the

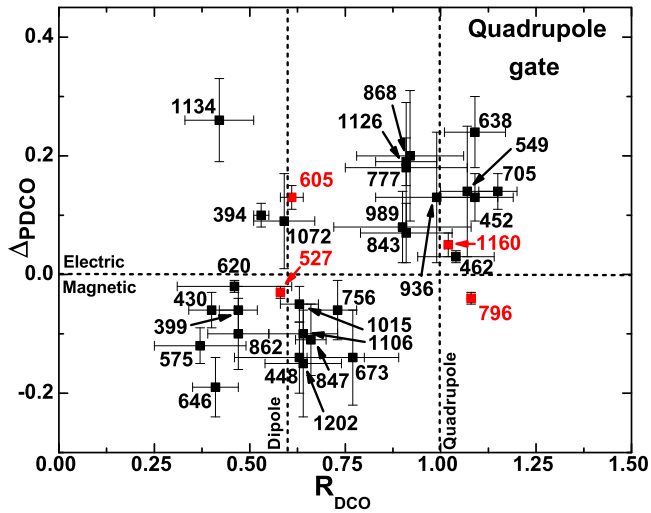

FIG. 3. DCO ratio ($R_{\rm DCO}$) vs. $\Delta_{\rm PDCO}$ plot of various new (black) and known (red) transitions observed in ^{117}Sb obtained in the present work. The DCO ratios shown in the plot are obtained in quadrupole gates only. The dotted lines at x axis are to guide the eye for the DCO ratio corresponding to pure dipole and quadrupole transitions, respectively. The dotted line at the y axis is to guide the eye for $\Delta_{\rm PDCO}$ values corresponding to the electric (+ve) and magnetic (−ve) nature of the transitions.

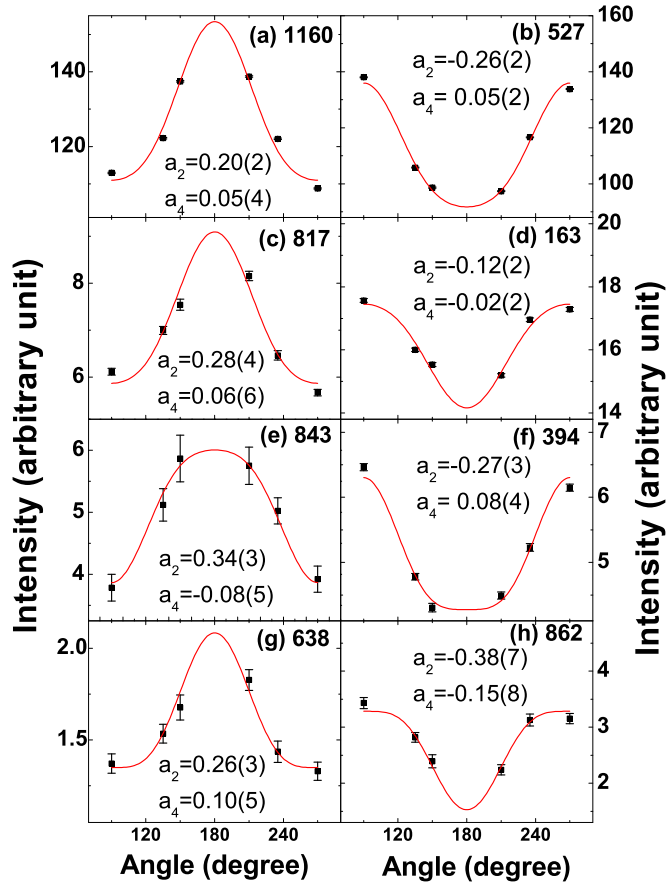

FIG. 4. Angular distribution of various transitions of ^{117}Sb observed in the present work. Panels (a), (c), (e), and (g) represent the distribution for quadrupole transitions and panels (b), (d), (f), and (h) represent distribution corresponding to dipole transitions in ^{117}Sb, as obtained in present work.

TABLE I. The energies (E_γ) and relative intensities (I_γ) of the γ rays observed in ^{117}Sb along with the spin and parity of the initial (J_i^π) and the final (J_f^π) states and the energy of the initial state (E_i). The measured values of $R_{\rm DCO}$ and $\Delta_{\rm PDCO}$ are also shown along with the multipolarity of the γ rays.

E_γ (keV)	E_i (keV)	$J_i^\pi \rightarrow J_f^\pi$	I_γ (Err)[a]	$R_{\rm DCO}$ (Err)	$\Delta_{\rm PDCO}$ (Err)	Multipolarity
(12)[b]	1323.1	$11/2^- \rightarrow 9/2^+$	–	–	–	$(E2)$
(16)[c]	3230.9	$23/2^- \rightarrow 19/2^-$	–	–	–	$(E2)$
155.2(1)	2780.8	$19/2^- \rightarrow 17/2^+$	0.27(2)	0.74(8)[d]	–	$E2$
163.0(1)	1323.1	$11/2^- \rightarrow 9/2^+$	0.18(2)	0.65(1)[d]	–	$E2$
181.1(1)	3174.9	$- \rightarrow 17/2^+$	0.05(2)	–	–	–
197.6(1)	3073.6	$21/2^- \rightarrow 19/2^-$	6.83(47)	0.67(1)[d]	−0.05(3)	$M1(+E2)$
202.3(1)	2525.9	$17/2^- \rightarrow 15/2^-$	11.24(78)	0.64(1)[d]	−0.04(2)	$M1(+E2)$
208.1(1)	3439.0	$25/2^- \rightarrow 23/2^-$	12.80(64)	0.67(3)[d]	–	$M1+E2$
221.4(1)	1310.8	$9/2^+ \rightarrow 7/2^+$	2.48(8)	1.15(4)[e]	–	$M1+E2$
250.4(1)	2876.0	$19/2^- \rightarrow 17/2^+$	0.87(6)	0.71(1)[d]	0.07(1)	$E2$
254.9(1)	2780.8	$19/2^- \rightarrow 17/2^-$	6.25(44)	0.83(1)[d]	−0.09(1)	$M1+E2$
279.8(1)	4031.2	$(23/2^+) \rightarrow 21/2^+$	0.10(8)	0.49(5)[d]	–	$(M1+E2)$
289.3(1)	1761.6	$9/2^+ \rightarrow 9/2^+$	1.27(5)	–	–	$(M1+E2)$
292.8(1)	3073.6	$21/2^- \rightarrow 19/2^-$	3.57(25)	0.82(1)[d]	−0.07(1)	$M1+E2$
293.3(1)	4199.3	$(23/2^+) \rightarrow 21/2^+$	0.09(4)	0.80(4)[d]	–	$(M1+E2)$
303.3(1)	3742.3	$27/2^- \rightarrow 25/2^-$	1.99(8)	1.15(2)[e]	−0.13(1)	$M1+E2$
334.7(2)	4761.3	$(27/2^+) \rightarrow 25/2^+$	0.21(8)	–	–	$(M1+E2)$
337.1(1)	1872.2	$13/2^+ \rightarrow 11/2^+$	23(2)	0.82(1)[d]	−0.09(1)	$M1+E2$
350.1(1)	2876.0	$19/2^- \rightarrow 17/2^-$	5.69(40)	0.81(3)[d]	−0.08(1)	$M1+E2$
366.1(1)	2238.3	$15/2^+ \rightarrow 13/2^+$	17(1)	0.81(2)[d]	−0.09(1)	$M1+E2$
366.9(1)	4109.2	$29/2^- \rightarrow 27/2^-$	1.16(5)	1.20(2)[e]	−0.13(2)	$M1+E2$
367.5(1)	2780.8	$19/2^- \rightarrow 15/2^-$	1.64(12)	1.08(3)[d]	0.09(2)	$E2$
371.9(1)	3214.9	$19/2^- \rightarrow 17/2^-$	0.88(16)	–	–	$(M1+E2)$
374.7(1)	1535.1	$11/2^+ \rightarrow 9/2^+$	35(2)	0.88(1)[d]	−0.09(1)	$M1+E2$
382.9(1)	1472.3	$9/2^+ \rightarrow 7/2^+$	0.40(8)	–	–	$M1+E2$
387.3(1)	2625.6	$17/2^+ \rightarrow 15/2^+$	12.27(85)	0.81(1)[d]	−0.07(1)	$M1+E2$
393.8(1)	3174.8	$21/2^+ \rightarrow 19/2^-$	0.64(11)	0.53(2)[d]	0.10(2)	$E2$
399.3(1)	1710.1	$11/2^+ \rightarrow 9/2^+$	0.75(6)	0.47(5)[d]	−0.06(4)	$M1+E2$
402.9(1)	4512.1	$31/2^- \rightarrow 29/2^-$	0.41(2)	1.12(3)[e]	−0.18(4)	$M1+E2$
413.9(2)	5175.2	$(29/2^+) \rightarrow (27/2^+)$	0.16(2)	0.50(11)[d]	−0.22(7)	$M1(+E2)$
423.4(1)	4426.6	$25/2^+ \rightarrow 23/2^+$	0.19(4)	0.68(4)[d]	−0.19(4)	$M1(+E2)$
425.8(1)	2187.4	$13/2^+ \rightarrow 9/2^+$	0.75(3)	1.02(2)[d]	0.08(2)	$E2$
428.1(1)	4940.2	$33/2^- \rightarrow 31/2^-$	0.17(2)	1.10(12)[e]	−0.16(3)	$M1(+E2)$
429.6(1)	3503.2	$23/2^- \rightarrow 21/2^-$	0.76(6)	0.40(6)[d]	−0.06(3)	$M1+E2$
429.7(1)	2843.0	$17/2^- \rightarrow 15/2^-$	0.66(6)	–	–	$(M1+E2)$
433.1(1)	3058.8	$19/2^+ \rightarrow 17/2^+$	4.45(35)	0.81(1)[d]	−0.06(1)	$M1+E2$
433.5(1)	2846.8	$19/2^- \rightarrow 15/2^-$	7.57(53)	0.99(1)[d]	0.11(1)	$E2$
434.1(1)	3214.9	$19/2^- \rightarrow 19/2^-$	0.45(4)	–	–	$(M1+E2)$[f]
448.3(1)	3441.9	$19/2^+ \rightarrow 17/2^+$	0.21(7)	0.63(17)[d]	−0.14(6)	$M1(+E2)$
452.1(1)	3626.9	$25/2^+ \rightarrow 21/2^+$	0.21(8)	1.09(10)[d]	0.13(4)	$E2$
457.2(1)	2780.8	$19/2^- \rightarrow 15/2^-$	4.03(28)	1.02(1)[d]	0.10(1)	$E2$
457.3(1)	5397.5	$35/2^- \rightarrow 33/2^-$	0.08(1)	1.21(6)[e]	−0.16(4)	$M1+E2$
462.1(1)	3904.0	$23/2^+ \rightarrow 19/2^+$	0.12(3)	1.04(10)[d]	0.03(1)	$E2$
462.7(1)	2876.0	$19/2^- \rightarrow 15/2^-$	1.17(8)	0.90(9)[d]	0.02(1)	$(E2)$
465.3(1)	3524.2	$21/2^+ \rightarrow 19/2^+$	2.74(19)	0.74(2)[d]	−0.12(2)	$M1+E2$
472.5(2)	5029.9	$27/2^+ \rightarrow 25/2^+$	0.19(5)	0.39(13)[d]	−0.11(6)	$M1+E2$
477.3(1)	2187.4	$13/2^+ \rightarrow 11/2^+$	0.59(3)	0.92(7)[e]	−0.08(4)	$M1(+E2)$
478.8(1)	4003.2	$23/2^+ \rightarrow 21/2^+$	0.94(7)	0.66(2)[d]	−0.14(1)	$M1(+E2)$
487.4(1)	2526.6	$15/2^+ \rightarrow 11/2^+$	0.74(13)	1.99(10)[e]	0.04(3)	$E2$
487.9(1)	5885.4	$37/2^- \rightarrow 35/2^-$	0.05(2)	1.14(10)[e]	−0.29(5)	$M1+E2$
511.4(1)	3742.3	$27/2^- \rightarrow 23/2^-$	–	–	–	$(E2)$
518.9(1)	6404.3	$(39/2^-) \rightarrow 37/2^-$	0.04(2)	–	–	$(M1+E2)$
519.4(1)	2843.0	$17/2^- \rightarrow 15/2^-$	1.19(9)	–	–	$(M1+E2)$[f]
523.2(2)	2846.8	$19/2^- \rightarrow 15/2^-$	0.69(5)	1.16(6)[d]	0.20(6)	$E2$
527.3(1)	527.3	$7/2^+ \rightarrow 5/2^+$	76(1)	0.58(1)[d]	−0.03(1)	$M1(+E2)$

TABLE I. (*Continued.*)

E_γ (keV)	E_i (keV)	$J_i^\pi \rightarrow J_f^\pi$	I_γ (Err)[a]	$R_{\rm DCO}$ (Err)	$\Delta_{\rm PDCO}$ (Err)	Multipolarity
534.9(1)	3061.5	$17/2^+ \rightarrow 15/2^+$	0.05(3)	–	–	$(M1+E2)$
547.7(1)	3073.6	$21/2^- \rightarrow 17/2^-$	0.54(4)	1.03(7)[d]	0.05(5)	$E2$
549.2(1)	3174.8	$21/2^+ \rightarrow 17/2^+$	0.56(4)	1.07(7)[d]	0.14(11)	$E2$
551.5(1)	2039.2	$11/2^+ \rightarrow 9/2^+$	6.11(25)	1.15(14)[e]	−0.05(4)	$M1+E2$
552.4(1)	2876.0	$19/2^- \rightarrow 15/2^-$	7.17(50)	0.98(1)[d]	0.07(3)	$E2$
554.2(2)	4557.4	$25/2^+ \rightarrow 23/2^+$	0.36(12)	0.76(17)[d]	–	$(M1+E2)$
570.8(1)	3417.6	$23/2^- \rightarrow 19/2^-$	4.15(29)	1.06(2)[d]	0.12(6)	$E2$
574.9(1)	4078.1	$25/2^- \rightarrow 23/2^-$	0.25(3)	0.37(12)[d]	−0.12(3)	$M1+E2$
589.3(1)	3214.9	$19/2^- \rightarrow 17/2^+$	3.22(23)	–	–	$(E2)$[f]
591.5(1)	2778.9	$17/2^+ \rightarrow 13/2^+$	5.65(40)	0.99(3)[d]	0.07(3)	$E2$
604.7(1)	2843.0	$17/2^- \rightarrow 15/2^+$	2.34(17)	–	–	$(E2)$[f]
607.5(1)	3838.4	$21/2^+ \rightarrow 19/2^+$	0.06(4)	–	–	$(M1+E2)$
608.2(1)	3389.0	$- \rightarrow 19/2^-$	0.70(6)	–	–	–
619.8(1)	3495.8	$21/2^- \rightarrow 19/2^-$	1.47(6)	0.46(15)[d]	−0.02(1)	$M1+E2$
632.8(1)	1160.4	$9/2^+ \rightarrow 7/2^+$	1.69(7)	1.12(3)[e]	−0.05(2)	$M1+E2$
637.5(1)	2993.6	$17/2^+ \rightarrow 13/2^+$	0.55(3)	1.09(8)[d]	0.24(6)	$E2$
646.0(1)	2356.1	$13/2^+ \rightarrow 11/2^+$	0.19(2)	0.41(6)[d]	−0.19(5)	$M1+E2$
670.2(1)	4109.2	$29/2^- \rightarrow 25/2^-$	0.18(2)	1.72(6)[e]	0.07(3)	$E2$
672.2(1)	1761.6	$9/2^+ \rightarrow 7/2^+$	8.81(32)	1.12(2)[e]	−0.02(2)	$M1+E2$
672.6(2)	3731.4	$21/2^+ \rightarrow 19/2^+$	0.21(2)	0.77(12)[d]	−0.14(8)	$M1+E2$
699.7(1)	2187.4	$13/2^+ \rightarrow 9/2^+$	1.59(7)	0.90(7)[d]	0.11(3)	$E2$
700.2(1)	4117.8	$27/2^- \rightarrow 23/2^-$	1.70(12)	1.02(2)[d]	0.05(3)	$E2$
703.2(1)	2238.3	$15/2^+ \rightarrow 11/2^+$	5.66(40)	1.04(1)[d]	0.04(1)	$E2$
704.3(1)	3230.9	$19/2^+ \rightarrow 15/2^+$	2.87(18)	1.10(3)[d]	0.08(3)	$E2$
705.4(1)	3061.5	$17/2^+ \rightarrow 13/2^+$	1.11(5)	1.15(5)[d]	0.14(3)	$E2$
707.5(1)	3486.4	$21/2^+ \rightarrow 17/2^+$	3.16(37)	1.05(7)[d]	0.08(2)	$E2$
711.8(1)	1872.2	$13/2^+ \rightarrow 9/2^+$	5.92(51)	1.01(1)[d]	0.07(1)	$E2$
753.4(1)	2625.6	$17/2^+ \rightarrow 13/2^+$	6.42(45)	0.95(2)[d]	0.05(1)	$E2$
755.5(1)	2993.8	$17/2^+ \rightarrow 15/2^+$	0.08(4)	0.73(5)[d]	−0.06(5)	$M1+E2$
769.8(1)	4512.1	$31/2^- \rightarrow 27/2^-$	0.17(1)	1.74(6)[e]	0.04(3)	$E2$
776.9(1)	3838.4	$21/2^+ \rightarrow 17/2^+$	0.38(2)	0.91(8)[d]	0.19(4)	$E2$
783.5(1)	1310.8	$9/2^+ \rightarrow 7/2^+$	3.59(15)	1.03(2)[e]	−0.02(1)	$M1(+E2)$
795.8(1)	1323.1	$11/2^- \rightarrow 7/2^+$	22(1)	1.08(1)[d]	−0.04(1)	$M2$
800.6(1)	4031.5	$23/2^+ \rightarrow 19/2^+$	1.08(5)	1.01(5)[d]	0.04(3)	$E2$
801.6(1)	3214.9	$19/2^- \rightarrow 15/2^-$	0.36(3)	–	–	$(E2)$
811.1(1)	4297.5	$25/2^+ \rightarrow 21/2^+$	1.33(11)	1.22(12)[d]	0.07(6)	$E2$
813.1(1)	4930.9	$31/2^- \rightarrow 27/2^-$	0.54(4)	0.96(4)[d]	0.10(3)	$E2$
816.5(1)	2526.6	$15/2^+ \rightarrow 11/2^+$	5.36(22)	1.02(2)[d]	0.09(1)	$E2$
820.5(1)	3058.8	$19/2^+ \rightarrow 15/2^+$	2.15(15)	1.06(3)[d]	0.02(1)	$E2$
831.0(1)	4940.2	$33/2^- \rightarrow 29/2^-$	0.11(1)	1.08(19)[d]	0.10(4)	$E2$
842.9(2)	4681.3	$25/2^+ \rightarrow 21/2^+$	0.23(2)	0.91(12)[d]	0.07(5)	$E2$
847.2(1)	3906.0	$21/2^+ \rightarrow 19/2^+$	0.12(3)	0.66(4)[d]	−0.11(6)	$M1(+E2)$
862.0(1)	4357.8	$23/2^- \rightarrow 21/2^-$	0.16(7)	0.47(8)[d]	−0.10(6)	$M1+E2$
868.4(1)	2356.1	$13/2^+ \rightarrow 9/2^+$	2.25(9)	0.92(14)[d]	0.20(11)	$E2$
871.4(1)	4902.9	$27/2^+ \rightarrow 23/2^+$	1.66(8)	1.07(9)[d]	0.02(2)	$E2$
876.6(1)	2187.4	$13/2^+ \rightarrow 9/2^+$	9.76(69)	1.06(2)[d]	0.07(1)	$E2$
885.4(1)	5397.5	$35/2^- \rightarrow 31/2^-$	0.09(1)	1.05(13)[d]	0.04(4)	$E2$
886.0(1)	5183.5	$29/2^+ \rightarrow 25/2^+$	0.19(3)	0.96(5)[d]	0.10(6)	$E2$
891.3(1)	3214.9	$19/2^- \rightarrow 15/2^-$	1.78(13)	–	–	$(E2)$[f]
898.4(1)	3524.2	$21/2^+ \rightarrow 17/2^+$	1.41(10)	0.97(4)[d]	0.16(3)	$E2$
902.4(1)	4426.6	$25/2^+ \rightarrow 21/2^+$	0.27(2)	1.00(11)[d]	0.11(6)	$E2$
907.8(1)	5838.7	$35/2^- \rightarrow 31/2^-$	0.18(2)	1.05(13)[d]	0.05(4)	$E2$
917.6(1)	2228.4	$11/2^+ \rightarrow 9/2^+$	2.91(21)	0.51(2)[d]	−0.05(3)	$M1(+E2)$
921.9(1)	5824.8	$31/2^+ \rightarrow 27/2^+$	0.09(3)	1.13(26)[d]	0.14(7)	$E2$
935.8(1)	3994.6	$23/2^+ \rightarrow 19/2^+$	0.18(2)	0.99(16)[d]	0.13(11)	$E2$
939.1(1)	6122.6	$33/2^{(+)} \rightarrow 29/2^+$	0.05(1)	1.15(33)[d]	–	$(E2)$
944.4(1)	4003.2	$23/2^+ \rightarrow 19/2^+$	0.94(7)	1.23(12)[d]	0.07(2)	$E2$

TABLE I. (*Continued.*)

E_γ (keV)	E_i (keV)	$J_i^\pi \rightarrow J_f^\pi$	I_γ (Err)[a]	R_{DCO} (Err)	Δ_{PDCO} (Err)	Multipolarity
945.2(1)	5885.4	$37/2^- \rightarrow 33/2^-$	0.03(1)	1.93(20)[e]	0.15(12)	$E2$
960.4(1)	1487.7	$9/2^+ \rightarrow 7/2^+$	7.99(32)	0.89(2)[e]	−0.02(1)	$M1+E2$
989.4(1)	3227.7	$19/2^+ \rightarrow 15/2^+$	0.16(2)	0.90(18)[d]	0.08(6)	$E2$
992.2(2)	6830.9	$39/2^- \rightarrow 35/2^-$	0.11(2)	0.96(19)[d]	0.08(6)	$E2$
1000.5(1)	2323.6	$15/2^- \rightarrow 11/2^-$	41(3)	0.94(2)[d]	0.03(1)	$E2$
1006.8(1)	6404.3	$(39/2^-) \rightarrow 35/2^-$	0.02(1)	–	–	$(E2)$
1008.9(1)	1536.2	$9/2^+ \rightarrow 7/2^+$	2.48(10)	1.07(4)[e]	−0.07(2)	$M1(+E2)$
1014.7(1)	4073.5	$21/2^+ \rightarrow 19/2^+$	0.47(4)	0.63(5)[d]	−0.05(3)	$M1(+E2)$
1026.7(2)	5029.9	$27/2^+ \rightarrow 23/2^+$	0.12(4)	1.21(34)[d]	0.26(14)	$E2$
1033.2(1)	4557.4	$25/2^+ \rightarrow 21/2^+$	0.27(8)	0.90(24)[d]	0.20(8)	$E2$
1045.3(1)	2356.1	$13/2^+ \rightarrow 9/2^+$	6.14(44)	1.05(3)[d]	0.05(2)	$E2$
1061.9(1)	2772.0	$15/2^+ \rightarrow 11/2^+$	0.06(2)	0.92(5)[d]	0.18(12)	$E2$
1072.1(1)	3697.7	$19/2^- \rightarrow 17/2^+$	0.33(2)	0.59(8)[d]	0.09(8)	$E2$
1076.8(1)	7907.7	$43/2^- \rightarrow 39/2^-$	0.11(3)	0.95(13)[d]	0.23(6)	$E2$
1089.4(1)	1089.4	$7/2^+ \rightarrow 5/2^+$	35(2)	0.30(2)[d]	−0.06(2)	$M1+E2$
1090.2(1)	2413.3	$15/2^- \rightarrow 11/2^-$	11.20(78)	0.98(2)[d]	0.04(1)	$E2$
1106.2(1)	3731.8	$19/2^+ \rightarrow 17/2^+$	0.34(3)	0.64(9)[d]	−0.10(5)	$M1(+E2)$
1125.8(2)	3751.4	$21/2^+ \rightarrow 17/2^+$	0.18(2)	0.91(16)[d]	0.18(11)	$E2$
1133.5(2)	3005.7	$15/2^- \rightarrow 13/2^+$	0.19(2)	0.42(9)[d]	0.26(7)	$E2$
1160.4(1)	1160.4	$9/2^+ \rightarrow 5/2^+$	100(1)	1.02(1)[d]	0.05(2)	$E2$
1182.8(1)	1710.1	$11/2^+ \rightarrow 7/2^+$	9.90(40)	1.10(3)[d]	0.02(1)	$E2$
1201.9(1)	3440.2	$17/2^+ \rightarrow 15/2^+$	0.51(4)	0.64(10)[d]	−0.15(9)	$M1(+E2)$
1234.3(1)	1761.6	$9/2^+ \rightarrow 7/2^+$	1.42(6)	0.93(3)[e]	−0.06(2)	$M1(+E2)$
1310.8(1)	1310.8	$9/2^+ \rightarrow 5/2^+$	27.73(29)	0.96(2)[d]	0.04(2)	$E2$
1323.1(1)	1323.1	$11/2^- \rightarrow 5/2^+$	67.62(94)	1.19(1)[d]	0.05(3)	$E2$
1472.3(1)	1472.3	$9/2^+ \rightarrow 5/2^+$	5.89(11)	1.27(19)[d]	0.11(6)	$E2$
1511.9(2)	2039.2	$11/2^+ \rightarrow 7/2^+$	1.02(5)	1.11(9)[d]	0.07(3)	$E2$
1536.2(1)	1536.2	$9/2^+ \rightarrow 5/2^+$	0.47(4)	–	–	$(E2)$
1761.6(1)	1761.6	$9/2^+ \rightarrow 5/2^+$	0.11(2)	1.26(22)[d]	–	$(E2)$

[a]Relative γ-ray intensities are estimated from the relevant coincidence gates of transitions feeding to the ground state and then normalized to the intensity of 1160.4-keV γ ray in prompt singles spectrum.
[b]Transition not observed in present work, adopted from Ref. [8].
[c]Transition not observed in present work, adopted from Ref. [20].
[d]From quadrupole gate.
[e]From dipole gate.
[f]Adopted from Ref. [20].

transitions of band B1 are determined from the 1183-keV ($E2$) gate and the positive Δ_{PDCO} value of these transitions together confirm this band as a positive-parity $E2$ band. The B1(a) sequence consists of four transitions of the energy 1045, 705, 777, and 843 keV, which are found to be of $E2$ character from the positive Δ_{PDCO} values and R_{DCO} measurements in the quadrupole gate from the present work. The interconnecting transitions between B1 and B1(a) are also established from the current work, which links these two bands into signature partners. B1(a) is found to decay to B1 via 608-, 535-, and 646-keV $M1$ transitions, as indicated in the level scheme (Fig. 2). On the other hand, only one transition of energy 399 keV is found to decay from the $11/2^+$ level of band B1 to the $9/2^+$ level of band B1(a). A coincidence spectra corresponding to the gate of the 817- and 1183-keV transitions of band B1 are shown in Figs. 5(a) and 5(b), respectively. The insets of Figs. 5(a) and 5(b) show the expanded part of the corresponding coincidence gates, from which the connecting $M1$ transitions between B1 and B1(a) are clearly seen. Another new sequence of transitions are seen above the 2356-keV level marked as B1(b) in the level scheme (Fig. 2). The 638-, 448-, and 462-keV transitions are the γ rays observed in this sequence. Among these, the 638- and 462-keV γ rays are found to be of $E2$ nature and the 448-keV γ ray is found to have $M1$ nature. The placement of these transitions in the sequence B1(b) are made on the basis of their relative intensities. The coincidence spectrum corresponding to the 1045-keV gate, showing the γ rays of B1(a) and the new γ rays of B1(b), is shown in Fig. 5(c).

In the present work, the bands B2 and B3 are observed up to $33/2^{(+)}$ and $43/2^-$, respectively. The spin-parity assignments of the 7908- $(43/2^-)$, 6831- $(39/2^-)$, and 5839- $(35/2^-)$ keV levels of band B3 are confirmed from the present work, which were reported as tentative in Ref. [7]. The strongly coupled negative-parity band structure, B4, is observed upto $(39/2^-)$ level in the present work. This level structure is built above the reported 290-ns isomeric state [20]. The higher-spin states beyond $25/2^-$ of this band was only tentatively assigned from the previous work [7]. From the present measurements of R_{DCO} and Δ_{PDCO}, the spin-parity

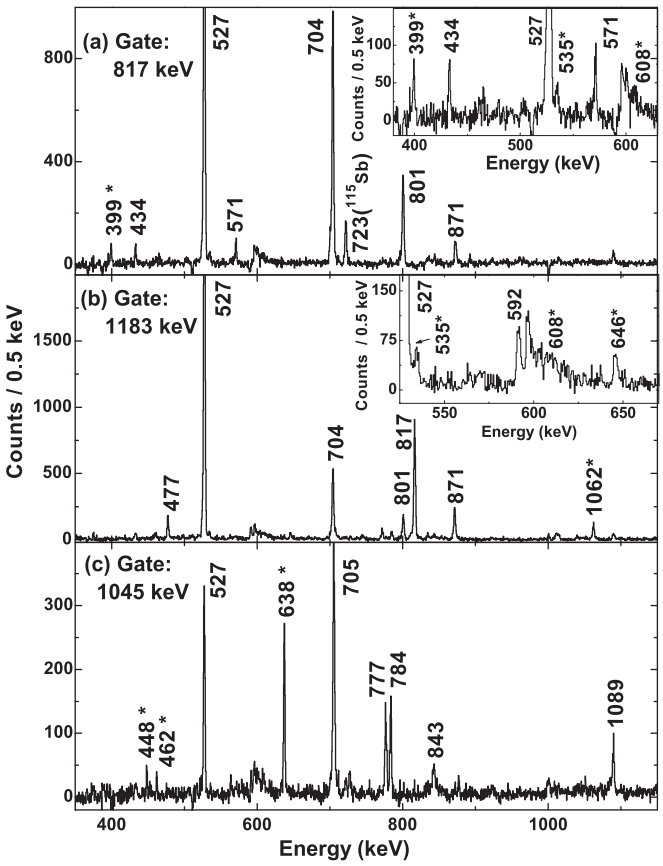

FIG. 5. Coincidence spectra corresponding to (a) the 817-keV gate of band B1, (b) the 1183-keV gate of band B1, and (c) the 1045-keV gate of band B1(a). The insets of (a) and (b) show the expanded view of the coincidence spectra of the 817- and 1183-keV gates, respectively. The newly observed transitions are marked with "∗."

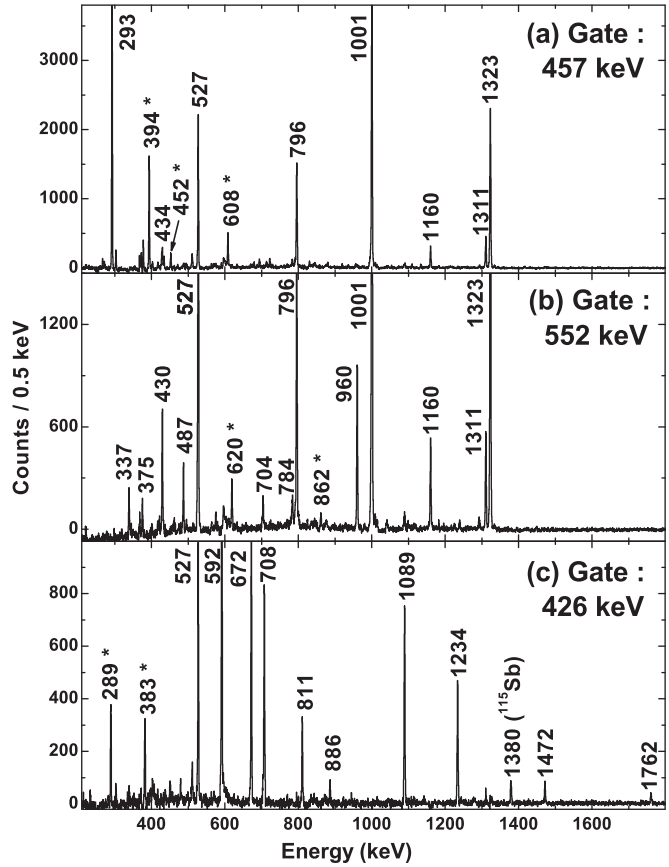

FIG. 6. Coincidence spectra corresponding to the gates of (a) 457-keV γ ray of B6(a), (b) 552-keV γ ray of B6(b), and (c) 426-keV γ ray of B2. The new γ rays observed in the present work are marked "∗."

assignment of these states could be firmly assigned, except for the $(39/2^-)$ level, as the multipolarities of the 1007- and 519-keV transitions, depopulating from this level, could not be deduced due to their weak intensities.

The band B5(a) is a strongly coupled positive-parity band interconnected with strong $M1 + E2$ transitions and observed upto $27/2^+$ level. The spin-parity assignments of the top two levels could be confirmed as $25/2^+$ and $27/2^+$ from the present $R_{\rm DCO}$ and $\Delta_{\rm PDCO}$ measurements. The dipole transitions of this band are found to be of mixed $(M1 + E2)$ character from their deduced $R_{\rm DCO}$ values. The sequence B5(b) is connected to the band B5(a) at $23/2^+$ level and is observed to $(29/2^+)$ from the present work. The transitions of the sequence B6 were also observed in Ref. [7] without any spin-parity assignment. From the current work, the $R_{\rm DCO}$ and $\Delta_{\rm PDCO}$ measurements of 430- and 575-keV γ rays confirm the spin-parity of the corresponding levels.

B6(a) and B6(b) as marked in the level scheme are the newly observed short sequences extended above the 2781-$(19/2^-)$ and 2876- $(19/2^-)$ keV levels, respectively. Two transitions of energy 394 and 452 keV are placed in the sequence B6(a) and 620- and 862-keV transitions are placed in the sequence B6(b). Another weak 608-keV transition is found to feed the 2781- $(19/2^-)$ keV level of sequence B6(a). Figures 6(a) and 6(b) represent the coincidence spectra corresponding to the gates of 457 keV of B6(a) and 552 keV of B6(b), respectively, as obtained from E_γ-E_γ matrix of the present work. The new transitions observed in these two sequences are marked with "∗" in Figs. 6(a) and 6(b). The set of nonyrast single-particle positive-parity states below 2.5 MeV, reported earlier [7,19], are also observed in the present work. Several interconnecting transitions between these states, such as 221, 289, 383, 868, 1234, and 1472 keV, are placed in the level scheme of ^{117}Sb from the E_γ-E_γ coincidence information obtained from the present work. Figure 6(c) shows the coincidence spectra corresponding to the gate of 426 keV, demonstrating the new transitions observed in coincidence. The assignment of these new transitions to the level scheme are carried out from their coincidence relationships and their multipolarities are obtained from the $R_{\rm DCO}$ and $\Delta_{\rm PDCO}$ measurements. Another transition of 918 keV, which is of $E2$ nature, is placed above the 1311-keV, $9/2^+$, level. It therefore fixes the spin-parity of the depopulating level as $11/2^+$. The two higher-energy transitions of 1536 and 1762 keV were reported earlier from the $(p, n\gamma)$ reaction [19] but not from the heavy-ion-induced reaction reported in Ref. [7]. However,

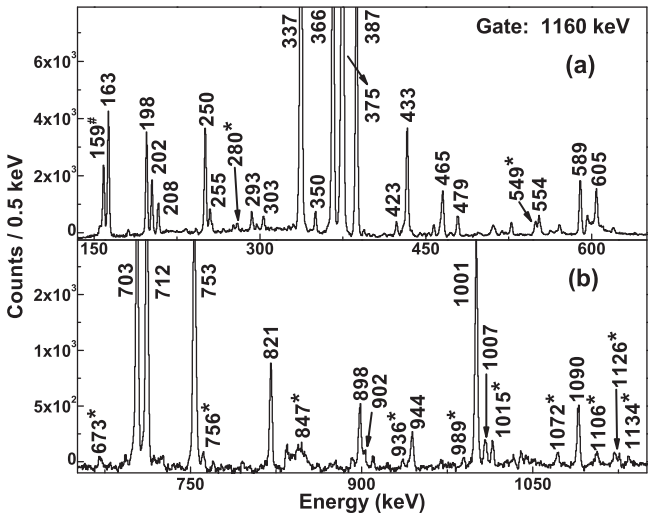

FIG. 7. Coincidence spectra corresponding to the gate of 1160-keV transition of band B5, (a) to 625 keV and (b) above 625 keV. All the newly observed transitions are marked with "∗." The 159 keV, marked with "#," is from ^{117}Sn, populated from the decay of ^{117}Sb.

these transitions are also observed in the present $(\alpha, 2n\gamma)$ reaction.

A new set of γ rays, connected to the various levels of band B5(a), are observed in the present work. Figure 7 represents the coincidence spectrum corresponding to the gate of 1160-keV transition. Newly observed γ rays from the present work are marked with "∗" along with the other known transitions of band B5(a). Placement of these γ rays in the level scheme and spin-parity assignments of the corresponding states are carried out based on the observed coincidence relationships, as well as from the deduced $R_{\rm DCO}$ and $\Delta_{\rm PDCO}$ values.

V. DISCUSSION

The nucleus ^{117}Sb, with one proton above the $Z = 50$ shell closure and neutrons at the middle of $N = 50$–82 shell, reveals various single-particle excitations at low spins and low excitation energies corresponding to all the possible coupling of the odd valence proton to the spherical and deformed structures of the ^{116}Sn core. The various low-lying states in ^{117}Sb are mainly attributed as to arise due to the odd valence proton occupying the orbitals above the $Z = 50$ shell, i.e., $\pi g_{7/2}$, $\pi d_{5/2}$, $\pi h_{11/2}$. In the present work, the main focus is on bands B1 and B1(a) which are based on the configuration involving $\pi g_{7/2}$ and are established as the signature partner bands. Apart from this, a number of new single-particle, nonyrast states have been reported in the low- and medium-spin regions. The connections between states originating from single-particle excitations and the states of the decoupled bands indicate mixing of various configurations at low spin. Other than these, a bandlike sequence B1(b) on top of the $13/2^+$ state [of the band B1(a)] and two short sequences B6(a) and B6(b) developed on top of the $15/2^-$ state, involving mainly the $\pi h_{11/2}$ contribution, have been identified for the first time in this work.

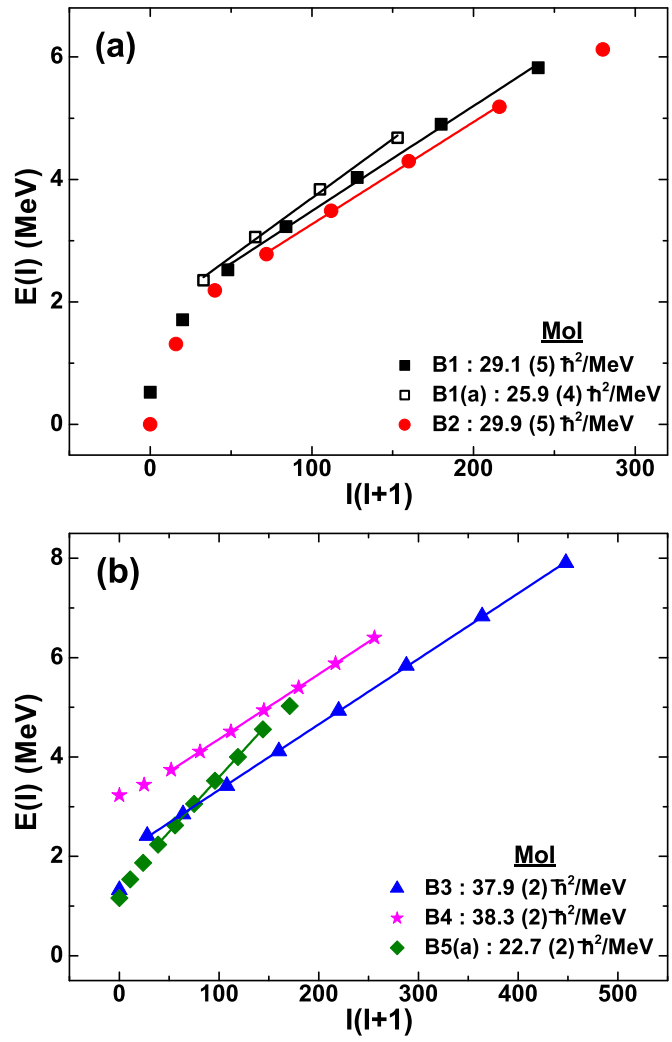

FIG. 8. Excitation energy $[E(I)]$ as a function of $I(I+1)$, for (a) bands B1, B1(a), and B2 and (b) bands B3, B4, and B5(a) of ^{117}Sb. I is the rotational angular momentum of the corresponding state. The lines are corresponding to the fits of the data with a linear function to obtain the MoI.

In order to investigate the nature of the bands B1 and B1(a), the level energies, $E(I)$, of these bands along with the other observed bands are plotted as a function of $I(I+1)$ in Figs. 8(a) and 8(b). In these plots, I is the rotational angular momentum of the corresponding state, obtained after subtracting the bandhead contribution from the total spin. As can be seen from these figures, all the band structures observed in ^{117}Sb show a linear dependency and fit well with the rotational model formula, $E(I) = E_0 + (\hbar^2/2\mathcal{J}) * I * (I+1)$, where $\mathcal{J}$ is the moment of inertia and E_0 is a parameter corresponding to the initial energy of the band. The different slopes of the fitted straight lines, representing different band structures, would correspond to different moments of inertia. The linear part of these plots corresponding to various bands are only fitted to obtain the Moment of Inertia (MoI). It can be seen from Fig. 8(a) that the excitation energy of the lower-spin members of the bands B1 and B1(a) do not fall in the same fitted straight line and thus indicate

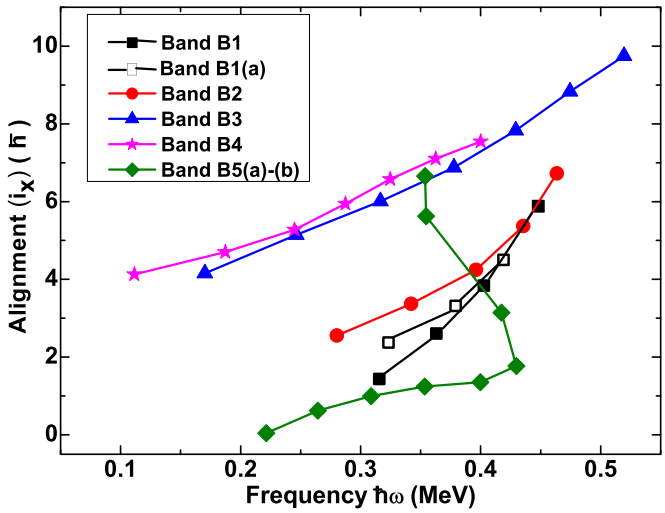

FIG. 9. Aligned angular momentum (i_x) of various band structures in ^{117}Sb as a function of rotational frequency $\hbar\omega$.

that these bands acquire rotational character from slightly higher spins. Though the bands B1 and B1(a) are built on the $7/2^+$ state, the pure bandlike structure develops above the $11/2^+$ level, which corresponds to the coupling of the $\pi g_{7/2}$ with the 2^+ state of the even-even core. This is similar to the bands B2 and B3 which involve $\pi d_{5/2}$ and $\pi h_{11/2}$ configurations and show bandlike sequences beyond $13/2^+$ and $15/2^-$ levels, respectively. Among the observed band structures, the bands B1, B2, and B5, involving single protons in $\pi g_{7/2}$, $\pi d_{5/2}$, and $\pi g_{9/2}$ configurations, have similar and smaller MoI, as expected. Among these, the strongly coupled $\pi g_{9/2}$ band has the lowest MoI. On the other hand, the band B3, involving single proton in $\pi h_{11/2}$, shows comparatively higher MoI, indicating higher deformation and, consequently, a larger shape-driving effect of the high-j $\pi h_{11/2}$ orbital compared to the positive-parity orbitals. The band B4 is built on the $23/2^-$ isomer with quasiparticle configuration of $[(\pi g_{7/2}d_{5/2})^2 \otimes (\pi g_{9/2})^{-1}] \otimes \nu 7^-$, where $\nu 7^-$ represents the $(\nu h_{11/2}d_{3/2})$ configuration of the 7^- state in the ^{116}Sn core. As expected, this five-quasiparticle band structure shows higher MoI.

The variation of the aligned angular momentum (i_x) as a function of rotational frequency ($\hbar\omega$) of the bands B1 and B1(a) along with the other bands in ^{117}Sb is shown in Fig. 9. These parameters were extracted from the experimental levels following the definitions of Ref. [29] and the Harris reference parameters of $J_0 = 17$ and $J_1 = 12$ have been used from Ref. [11]. It can be seen from this figure that bands B1 and B1(a) have similar aligned angular momentum (i_x), as expected for signature partner bands. The initial alignment of the band B5 is much less as it is based on a high-Ω orbital, whereas the intial alignment of the band B3 has been found to be higher and comparable to that of the five-quasiparticle band B5 as the band B3 is based on the low-Ω component of the high-j, $\pi h_{11/2}$ orbital. It is interesting to note that band B2 with the $\pi d_{5/2}$ configuration has somewhat higher initial i_x than in bands B1 and B1(a).

A. PRM calculation for signature partner bands

In an attempt to understand the nature of bands B1 and B1(a) and to investigate the signature splitting between these two partner bands, Particle Rotor Model (PRM) calculations, incorporating the Variable Moment of Inertia (VMI) formalism [30], have been performed. The model is based on the assumption that the nucleus under consideration is axially symmetric and the motion of the unpaired quasiparticle moving in Nilsson's deformed orbital is coupled to the rotational motion through the Coriolis interaction. The theoretical study shows that the bands are based on a low-Ω Nilsson orbital, dominated largely by a $\pi g_{7/2}$ proton state with deformation $\beta_2 \approx 0.15$. The parameters μ and κ, used in the present calculation, have been suitably chosen [31] to obtain the best fit for the nuclei in this mass region. The Fermi level has been chosen close to 1/2[431], a down-sloping (for prolate deformation) Nilsson orbital, to obtain the best fit to the experimental data. The elastic constant of the VMI model gives reasonable fit with a value of 0.8×10^7 keV^3 signifying that the nucleus is not particularly soft toward deformation.

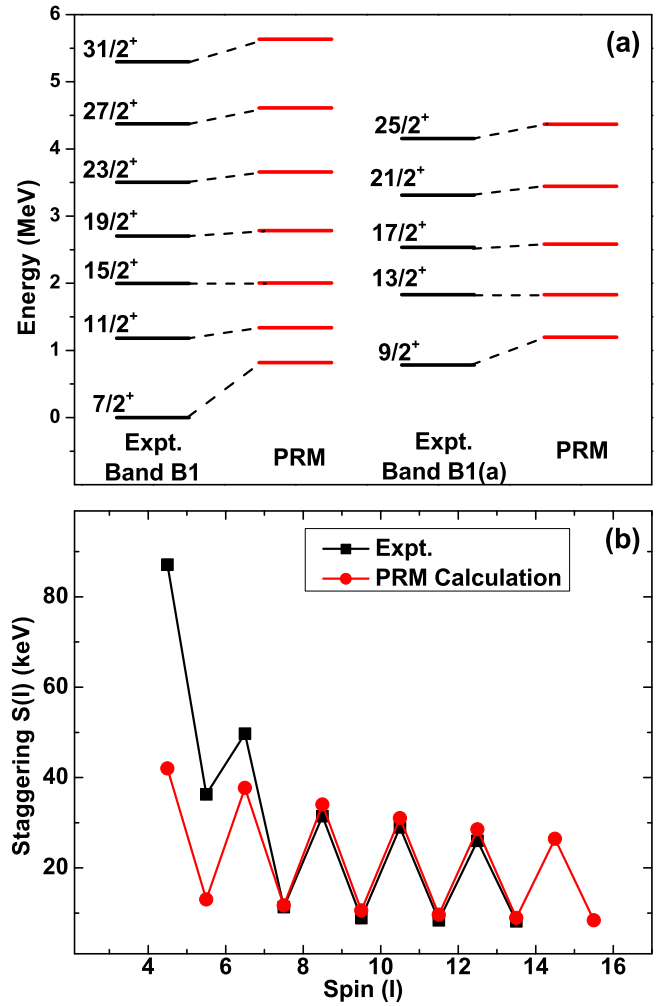

FIG. 10. Comparison of the experimental (a) energy levels and (b) energy staggering of bands B1 and B1(a) with that obtained from present PRM calculations. The energy levels are plotted with respect to the $13/2^+$ state.

The results of the theoretical calculations have been compared with the experimental data in Figs. 10(a) and 10(b). The calculated level energies are compared in Fig. 10(a) with respect to the $13/2^+$ state. It can be seen that the theory overestimates the low-lying experimental levels but is extremely successful in reproducing the experimental data above $11/2^+$ state. This is also consistent with the fact that the lower-spin members of the bands B1 and B1(a) have significant mixing of different configurations, as mentioned earlier, and do not follow the rotational behavior. The theoretical calculations also show large energy splitting between the signature partners with strong Coriolis interaction. The energy staggering, defined by $S(I) = [E(I) - E(I-1)]/2I$, where $E(I)$ is the energy of the state with spin I, is plotted as a function of spin (I) for the bands B1 and B1(a) in Fig. 10(b). As can be seen from this figure, an excellent agreement is obtained between the measured and the calculated data but again except for the first few state. Therefore, it is understood that the $\pi g_{7/2}$ orbital induces axial deformation to the even-even Sn core albeit assisted by the coupling with its 2^+ configuration.

B. Shell-model calculation for single-particle excitations

The low-spin-level structures in ^{117}Sb are generated from the single-particle excitations of the valence proton and the neutrons to the available orbitals above $Z = 50, N = 64$ core. The new positive-parity states observed below 2 MeV are mostly due to the single-particle excitations involving the odd proton above $Z = 50$ and its coupling to the spherical single-particle states in the corresponding ^{116}Sn core. The large basis shell-model calculations were carried out using the code OXBASH [32]. The SN100PN effective interaction [33] was used for the calculations. The model space for this calculation consists of orbitals of $Z, N = 50$–82 shell, viz., $g_{7/2}$, $d_{5/2}$, $d_{3/2}$, $s_{1/2}$, and $h_{11/2}$ for both protons and neutrons with ^{100}Sn taken as the core. Therefore, as the $g_{9/2}$ proton orbital, situated below the $Z = 50$ gap, has not been considered, the $9/2^+$ state in the band B5(a) will not be produced in this calculation.

The calculations were carried out with no restriction in the model space for the valence proton but for the neutrons the model space was truncated in such a way that the $\nu g_{7/2}$ orbital is always filled and no particle is placed in the $\nu h_{11/2}$ orbital. This restriction in neutron space is reasonable as the present calculation is carried out for the low-spin structures, where odd protons above the $Z = 50$ core are expected to play the major role. Figure 11 represents the comparison of the experimentally observed low-lying positive-parity states in ^{117}Sb with those obtained from the shell model (SM) calculations. It is evident from Fig. 11 that the experimental positive-parity states are reproduced reasonably well in the present shell-model calculations, except for the first $9/2^+$ and the first $11/2^+$ states. These states are underpredicted by about 500 keV. It may be noted that these two states are also part of the rotational bands but are affected by the coexisting structures of spherical and deformed shapes. The major contributions of the configurations for a particular state

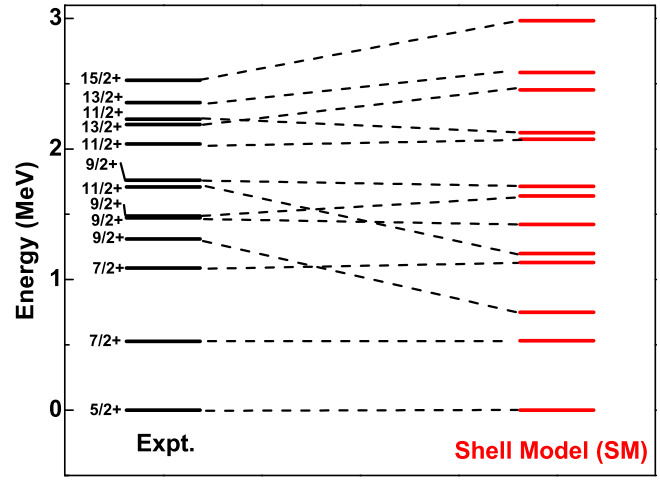

FIG. 11. Comparison of the experimentally observed low-lying states with that of the shell model calculation.

are shown in Table II. As can be seen from this table, the configuration for the $5/2^+$ ground state is dominated by one valence proton occupying the $\pi d_{5/2}$ orbital, and the last two valence neutrons in either $\nu d_{3/2}$ or $\nu s_{1/2}$ orbital, coupled to zero. The $7/2^+$ state at 527 keV, above which the signature partner bands B1 and B1(a) are built, has the contribution of $\pi g_{7/2}$ orbital with the neutron distribution same as that for the $5/2^+$ ground state. Table II shows that from the $13/2^+$ (2356 keV) member of signature partner bands B1 and B1(a), the configuration of the states are comparatively more pure, dominated by the major contribution of the partition $\pi(g_{7/2})^1 \otimes \nu[(d_{5/2})^5(d_{3/2})^1(s_{1/2})^2]$.

The newly observed set of levels, decaying to the various states of band B5(a), are not considered in the present shell-model calculations. Band B5(a) is known to have the 2p-1h configuration of $[(\pi g_{7/2})^2 \otimes (\pi g_{9/2})^{-1})]$, involving proton hole excitation across $Z = 50$ core. Thus, the new set of levels, connecting to band B5 will also involve the above 2p-1h configuration. Such particle-hole excitation to the $\pi g_{9/2}$ orbital is not within the scope of the present shell-model calculation.

VI. SUMMARY

In summary, the rotational band structures and the low-lying single-particle excitations in ^{117}Sb have been studied using the fusion evaporation reaction ^{115}In$(\alpha, 2n)$ ^{117}Sb at the beam energy of 28 MeV and the VENUS setup with six Compton suppressed Clover HPGe detectors and a digital data acquisition system. The level scheme of ^{117}Sb is extended with the placement of 31 new γ transitions. The signature partner of the band, based on $\pi g_{7/2}$ configuration coupled to the 2p-2h structure of the ^{116}Sn core, has been established for the first time in ^{117}Sb, from the observation of connecting $M1$ transitions and the firm assignment of the spin and parity of the states in these bands. The spin-parity of most of the states are assigned, based on the DCO ratio, angular distribution, and polarization asymmetry measurements. The rotational

TABLE II. Experimental excitation energy (E_x) and spin (J^π) and their calculated configurations with % contribution ($\geqslant$10%) of the positive-parity low-lying states in ^{117}Sb, as obtained from shell-model calculations.

Spin (J^π)	E_x (Expt.) (in keV)	Configuration	Contribution
$5/2^+$	0	$\pi(d_{5/2})^1 \otimes \nu[(d_{5/2})^6(s_{1/2})^2]$	37%
		$\pi(d_{5/2})^1 \otimes \nu[(d_{5/2})^6(d_{3/2})^2]$	36%
$7/2^+$	527	$\pi(g_{7/2})^1 \otimes \nu[(d_{5/2})^6(s_{1/2})^2]$	51%
		$\pi(g_{7/2})^1 \otimes \nu[(d_{5/2})^6(d_{3/2})^2]$	27%
$7/2^+$	1089	$\pi(d_{5/2})^1 \otimes \nu[(d_{5/2})^6(d_{3/2})^1(s_{1/2})^1]$	69%
		$\pi(d_{5/2})^1 \otimes \nu[(d_{5/2})^5(d_{3/2})^2(s_{1/2})^1]$	19%
$9/2^+$	1311	$\pi(d_{5/2})^1 \otimes \nu[(d_{5/2})^6(d_{3/2})^1(s_{1/2})^1]$	64%
		$\pi(d_{5/2})^1 \otimes \nu[(d_{5/2})^6(d_{3/2})^2]$	16%
$9/2^+$	1472	$\pi(g_{7/2})^1 \otimes \nu[(d_{5/2})^6(d_{3/2})^1(s_{1/2})^1]$	78%
		$\pi(g_{7/2})^1 \otimes \nu[(d_{5/2})^5(d_{3/2})^2(s_{1/2})^1]$	10%
$9/2^+$	1488	$\pi(d_{5/2})^1 \otimes \nu[(d_{5/2})^6(d_{3/2})^2]$	43%
		$\pi(g_{7/2})^1 \otimes \nu[(d_{5/2})^6(d_{3/2})^1(s_{1/2})^1]$	20%
		$\pi(d_{5/2})^1 \otimes \nu[(d_{5/2})^6(d_{3/2})^1(s_{1/2})^1]$	12%
$9/2^+$	1762	$\pi(g_{7/2})^1 \otimes \nu[(d_{5/2})^6(d_{3/2})^1(s_{1/2})^1]$	30%
		$\pi(g_{7/2})^1 \otimes \nu[(d_{5/2})^6(d_{3/2})^2]$	20%
		$\pi(d_{5/2})^1 \otimes \nu[(d_{5/2})^6(d_{3/2})^2]$	16%
		$\pi(g_{7/2})^1 \otimes \nu[(d_{5/2})^5(d_{3/2})^2(s_{1/2})^1]$	10%
$11/2^+$	1710	$\pi(g_{7/2})^1 \otimes \nu[(d_{5/2})^6(d_{3/2})^1(s_{1/2})^1]$	66%
		$\pi(g_{7/2})^1 \otimes \nu[(d_{5/2})^6(d_{3/2})^2]$	16%
$11/2^+$	2039	$\pi(g_{7/2})^1 \otimes \nu[(d_{5/2})^6(d_{3/2})^2]$	70%
		$\pi(g_{7/2})^1 \otimes \nu[(d_{5/2})^6(d_{3/2})^1(s_{1/2})^1]$	15%
$11/2^+$	2228	$\pi(d_{5/2})^1 \otimes \nu[(d_{5/2})^5(d_{3/2})^1(s_{1/2})^2]$	67%
		$\pi(d_{5/2})^1 \otimes \nu[(d_{5/2})^5(d_{3/2})^3]$	12%
$13/2^+$	2187	$\pi(d_{5/2})^1 \otimes \nu[(d_{5/2})^5(d_{3/2})^1(s_{1/2})^2]$	71%
		$\pi(d_{5/2})^1 \otimes \nu[(d_{5/2})^5(d_{3/2})^2(s_{1/2})^1]$	10%
$13/2^+$	2356	$\pi(g_{7/2})^1 \otimes \nu[(d_{5/2})^5(d_{3/2})^1(s_{1/2})^2]$	72%
		$\pi(g_{7/2})^1 \otimes \nu[(d_{5/2})^5(d_{3/2})^2(s_{1/2})^1]$	10%
$15/2^+$	2526	$\pi(g_{7/2})^1 \otimes \nu[(d_{5/2})^5(d_{3/2})^1(s_{1/2})^2]$	78%
		$\pi(g_{7/2})^1 \otimes \nu[(d_{5/2})^5(d_{3/2})^2(s_{1/2})^1]$	11%

nature, and thereby the deformed structure of bands B1 and B1(a), has been established from above the $11/2^+$ state by comparing with the rotational model. A $\pi g_{7/2}$ configuration has been assigned for this decoupled band with large signature splitting. The level energies and the signature splitting have been well reproduced by PRM calculations and indicate a low-Ω $\pi 1/2[431]$ Nilsson configuration for this band which is consistent with its large signature splitting. Several new nonyrast levels have been identified at low and medium spin. The low-lying positive-parity states have been interpreted in terms of large-scale shell model calculations.

ACKNOWLEDGMENTS

The authors thank the K-130 cyclotron operators at VECC, Kolkata, for providing a good-quality stable α beam. R.B. acknowledges with thanks the financial support received from the Department of Atomic Energy (DAE), Government of India. R.G. and D.C. acknowledge the support received from the project UGC-DAE-CSR-KC/CRS/13/NP07 funded by UGC-DAE-CSR-KC. The authors acknowledge technical support of A. Chowdhury, P. Mukhopadhyay, and I. Shaik of VECC, Kolkata, and K. Basu from UGC-DAE CSR, Kolkata Centre, during the experiment.

[1] K. Heyde, P. V. Isacker, M. Waroquier, J. L. Wood, and R. A. Meyer, Phys. Rep. **102**, 291 (1983).

[2] K. Heyde, M. Waroquier, H. Vincx, and P. V. Isacker, Phys. Lett. B **64**, 135 (1976).

[3] A. Savelius, S. Juutinen, K. Helariutta, P. Jones, R. Julin, P. Jämsen, M. Muikku, M. Piiparinen, J. Suhonen, S. Törmänen, R. Wyss, P. T. Greenlees, P. Simecek, and D. Cutoiu, Nucl. Phys. A **637**, 491 (1998).

[4] D. R. LaFosse, D. B. Fossan, J. R. Hughes, Y. Liang, H. Schnare, P. Vaska, M. P. Waring, J.-Y. Zhang, R. M. Clark, R. Wadsworth, S. A. Forbes, E. S. Paul, V. P. Janzen, A. Galindo-Uribarri, D. C. Radford, D. Ward, S. M. Mullins, D. Prévost, and G. Zwartz, Phys. Rev. C **50**, 1819 (1994).
[5] P. Banerjee, S. Ganguly, M. K. Pradhan, H. P. Sharma, S. Muralithar, R. P. Singh, and R. K. Bhowmik, Phys. Rev. C **87**, 034321 (2013).
[6] R. S. Chakrawarthy and R. G. Pillay, Phys. Rev. C **54**, 2319 (1996).
[7] D. R. LaFosse, D. B. Fossan, J. R. Hughes, Y. Liang, H. Schnare, P. Vaska, M. P. Waring, and J.-Y. Zhang, Phys. Rev. C **56**, 760 (1997).
[8] R. E. Shroy, A. K. Gaigalas, G. Schatz, and D. B. Fossan, Phys. Rev. C **19**, 1324 (1979).
[9] A. K. Gaigalas, R. E. Shroy, G. Schatz, and D. B. Fossan, Phys. Rev. Lett. **35**, 555 (1975).
[10] J. Bron, W. H. A. Hesselink, A. V. Poelgeest, J. J. A. Zalm-stra, M. J. Uitzinger, H. Verheul, K. Heyde, M. Waroquier, H. Vincx, and P. V. Isacker, Nucl. Phys. A **318**, 335 (1979).
[11] V. P. Janzen, H. R. Andrews, B. Haas, D. C. Radford, D. Ward, A. Omar, D. Prevost, M. Sawicki, P. Unrau, J. C. Waddington, T. E. Drake, A. Galindo-Uribarri, and R. Wyss, Phys. Rev. Lett. **70**, 1065 (1993).
[12] D. R. LaFosse, D. B. Fossan, J. R. Hughes, Y. Liang, P. Vaska, M. P. Waring, and J.-Y. Zhang, Phys. Rev. Lett. **69**, 1332 (1992).
[13] S. Tormanen, S. Juutinen, R. Julin, A. Lampinen, E. Makela, M. Piiparinen, A. Savelius, A. Virtanen, G. B. Hagemann, Ch. Droste, W. Karczmarczyk, T. Morek, J. Srebrny, and K. Starosta, Nucl. Phys. A **613**, 282 (1997).
[14] S. Ohya, Nucl. Data Sheets **111**, 1619 (2010).
[15] G. Berzins W. H. Kelly, G. Graeffe, and W. B. Walters, Nucl. Phys. A **104**, 241 (1967).
[16] W. D. Fromm, H. F. Brinckmann, F. Donau, C. Heiser, F. R. May, V. V. Pashkevich, and H. Rotter, Nucl. Phys. A **243**, 9 (1975).
[17] Yu. N. Lobach and D. Bucurescu, Phys. Rev. C **58**, 1515 (1998).
[18] Yu. N. Lobach and V. V. Trishin, Phys. Atom. Nucl. **58**, 1079 (1995).
[19] D. Bucurescu, I. Căta-Danil, G. Ilaş, M. Ivaşcu, L. Stroe, and C. A. Ur, Phys. Rev. C **52**, 616 (1995).
[20] M. Ionescu-Bujor, A. Iordachescu, G. Pascovici, and C. Stan-Sion, Nucl. Phys. A **466**, 317 (1987).
[21] Soumik Bhattacharya, R. Banik, S. S. Alam, A. Saha, Md. A. Asgar, T. Roy, A. Chowdhury, I. Seikh, P. Mukhopadhyay, A. Dhal, T. Bhattacharjee, S. Bhattacharyya, G. Mukherjee, S. Mukhopadhyay, D. Mondal, D. Pandit, S. Pal, and S. R. Banerjee, Proc. DAE-BRNS Symp. Nucl. Phys. **61**, 98 (2016).
[22] Soumik Bhattacharya, S. Bhattacharyya, R. Banik, S. Das Gupta, G. Mukherjee, A. Dhal, S. S. Alam, M. A. Asgar, T. Roy, A. Saha, S. Nandi, T. Bhattacharjee, A. Choudhury, D. Mondal, S. Mukhopadhyay, P. Mukhopadhyay, S. Pal, D. Pandit, I. Shaik, and S. R. Banerjee, Phys. Rev. C **98**, 044311 (2018).
[23] S. Das, S. Samanta, R. Banik, R. Bhattacharjee, K. Basu, R. Raut, S. S. Ghugre, A. K. Sinha, S. Bhattacharya, S. Imran, G. Mukherjee, S. Bhattacharyya, A. Goswami, R. Palit, and H. Tan, Nucl. Instrum. Methods A **893**, 138 (2018).
[24] D. C. Radford, Nucl. Instrum. Methods A **361**, 297 (1995).
[25] http://www.tifr.res.in/~pell/lamps.html.
[26] A. Kramer-Flecken *et al.*, Nucl. Instrum. Methods A **275**, 333 (1989).
[27] K. Starosta *et al.*, Nucl. Instrum. Methods A **423**, 16 (1999).
[28] Ch. Droste *et al.*, Nucl. Instrum. Methods A **378**, 518 (1996).
[29] R. Bengtsson and S. Frauendorf, Nucl. Phys. A **327**, 139 (1979).
[30] S. Bhattacharya, S. Sen, and R. K. Guchhait, Phys. Rev. C **32**, 1026 (1985).
[31] J.-Y. Zhang, N. Xu, D. B. Fossan, Y. Liang, R. Ma, and E. S. Paul, Phys. Rev. C **39**, 714 (1989).
[32] B. A. Brown *et al.*, Oxbash for Windows, MSU-NSCL Report No. 1289 (2004).
[33] B. A. Brown, N. J. Stone, J. R. Stone, I. S. Towner, and M. Hjorth-Jensen, Phys. Rev. C **71**, 044317 (2005).